Chemical Engineering Journal 420 (2021) 129895

Contents lists available at ScienceDirect

Chemical Engineering Journal

journal homepage: www.elsevier.com/locate/cej

Investigating the effect of diverse structural variation of conjugated polymer electrolytes as the interlayer on photovoltaic properties

Sabrina Aufar Salma [a], Mijin Jeong [a], Doo Kyung Moon [b], Joo Hyun Kim [a,*]

[a] Department of Polymer Engineering, Pukyong National University, Busan 48513, South Korea
[b] Division of Chemical Engineering, Konkuk University, Seoul 05029, South Korea

ARTICLE INFO

Keywords:
Conjugated polymer electrolyte
Cathode buffer layer
Transfer matrix formalism
DFT calculation
Inverted polymer solar cell

ABSTRACT

A series of conjugated polymer electrolytes (CPEs) based on dimethylamino propyl fluorene (FN), thiophene (T), benzothiadiazole (BT), and dithienyl benzothiadiazole (TBT) were synthesized by the Suzuki coupling reaction. Quaternarized polyelectrolytes were obtained from the post-polymerization treatment of the amino-terminal group. The incorporation of electron-rich (T), electron-deficient moiety (BT), and their combination (TBT) in the polymer backbone represent the different effects of polarity. Conjugated backbones are substantially strengthened by varying their electron affinity and conjugated planarity. We systematically investigated the effect of applying CPEs with different backbones and functionalities in the side chain. Different backbones produce different molecular dipoles, and the side chain functionality induces an interfacial dipole. Inverted polymer solar cells (iPSCs) based on a bulk heterojunction (BHJ) were fabricated with the ITO/ZnO/CPE/PTB7-Th:$PC_{71}BM$/MoO_3/Ag structure. The device performance enhancement was achieved by inserting CPEs as the interlayer. Modifying the polymer backbone leads to improved efficiency and modifying the side chain functionality improves the performance compared with that of the interlayered neutral polymer.

1. Introduction

Polymer solar cells (PSCs) are a promising alternative source of clean and renewable energy. In recent decades, PSCs have been extensively investigated owing to their mechanical flexibility, low weight, low-cost energy sources, large-scale fabrication, and roll-to-roll printing [1-8]. As an emerging photovoltaic technology, PSCs based on the combination of an electron donor and electron acceptor with a bulk heterojunction (BHJ) are advantageous over the conventional device structure [9-12]. The idea of BHJ was introduced by Yu et al. [13,14], wherein the blending donor (D) and acceptor (A) materials were very close to each other, typically less than 10 nm apart. Such distances are within the exciton pair mean free-path lengths (the minimum diffusion distance before the exciton can be annihilated via recombination) [15,16]. An interpenetrating network with a large donor–acceptor interfacial area can be achieved by controlling the phase separation between the two bulk components, resulting in efficient charge collection [15,17]. Therefore, the present PSC studies are focused on enhancing the device power conversion efficiency (PCE). Selectively or simultaneously enhancing the short-circuit current (J_{SC}), open-circuit voltage (V_{OC}), and fill factor (*FF*) are critical to increasing PCE. The J_{SC} is determined by the bandgap, thickness, morphology, and breadth of the absorption band of the active layer materials. These parameters influence the charge transport to the electrodes [18]. Additionally, the V_{OC} can be increased by tuning either the lowest unoccupied molecular orbital (LUMO) or the highest occupied molecular orbital (HOMO) energy levels of the acceptors or polymer donors, respectively [19]. The *FF* can be increased by improving the active layer morphologies for balanced charge transport [20-23].

In addition to the synthesis of photoactive materials, interlayer modification is essential for solving the intrinsic limitations of mismatched energy levels, unbalanced carrier mobility, and improved device efficiency and stability in PSCs.[12-14] Interfacial engineering is a fundamental approach to increasing PCEs [17,24-29]. The anode/cathode buffer layers are inserted between the active layer and the electrodes. These buffers can alleviate the interfacial energy barriers and facilitate charge transporting/collection capability when holes are collected at the anode and electrons are extracted at the cathode [30]. Appropriate materials could efficiently hamper charge recombination and lower contact resistance at the active layer/electrode interface, leading to enhanced hole/electron extraction. As a result, J_{SC}, V_{OC}, and *FF*, in a single device, can be selectively or simultaneously enhanced

* Corresponding author.
E-mail address: jkim@pknu.ac.kr (J.H. Kim).

https://doi.org/10.1016/j.cej.2021.129895
Received 25 January 2021; Received in revised form 29 March 2021; Accepted 13 April 2021
Available online 20 April 2021

[31].

Among the many material types used as interlayer materials in PSCs, conjugated polymer electrolytes (CPEs) have been reported to improve the PCE. CPEs consist of a conjugated polymer backbone and a polar ionic side group. Alcohol-soluble CPEs are efficient interfacial materials owing to their unique properties [28]. These properties include intimate contact with the hydrophobic organic active layer and hydrophilic electrode alcohol-soluble fabrication without intermixing with the halogenated solvent-processed active layer [8,32-34]. The alcohol-soluble CPE forms an interfacial dipole at the cathode interface and improves the built-in electrical field [35,36]. Therefore, many high-performance fluorene-based CPEs, such as the widely used PFN (poly[(9,9-bis (3-(N,N-dimethylamino) propyl)-2,7-fluorene)-alt-2,7-(9,9-dioctyl fluorene)]), contain hydrophilic amino groups and hydrophobic aliphatic side chains [37-40].

In this study, we designed and synthesized diverse CPEs to investigate the effect of their backbone and side chain structures, based on dimethylaminopropyl fluorene (FN) interlayer, on photovoltaic properties. Fig. 1 shows a series of CPEs with different side chains divided into three categories. The first category contains FN polymers as a neutral precursor (neutral polymer category) with an FN backbone with a thiophene named PFN-T (poly[(9,9-bis(3′-(N,N-dimethylamino)propyl)-2,7-fluorene)-alt-4,7-(thiophene)]); an FN backbone with a benzothidiazole named PFN-BT (poly[(9,9-bis(3′-(N,N-dimethylamino) propyl)-2,7-fluorene)-alt-4,7-(2,1,3-benzothiadiazole)]); and an FN backbone with a dithienyl-benzothiadiazole unit named PFN-TBT (poly- [(9,9-bis(3′-(N,N-dimethylamino)propyl)-2,7-fluorene)-alt-4,7-(dithienyl)-2,1,3 (benzothiadiazole)]). The second category contains FN polymer derivatives (salt polymer category) quaternarized with a tetraalkyl ammonium salt named PFN-T salt (poly[(9,9-bis(3′-(N-ethy-N,N-dimethylamino)propyl)dibromide-2,7-fluorene)-alt-4,7 (thiophene)]); PFN-BT salt (poly[(9,9-bis(3′-(N-ethyl-N,N-dimethylamino) propyl)dibromo-2,7-fluorene)-alt-4,7-(2,1,3 benzothiadiazole)]); and PFN-TBT salt (poly-[(9,9-bis(3′-(N-ethyl,N,N-dimethylamino) propyl) dibromide-2,7-fluorene)-alt-4,7-(dithienyl)-2,1,3(benzothia-diazole)]). The last category contains neutral polymers quaternarized with an ethyl hydroxy trialkyl ammonium salt (OH salt polymer category) named PFN-T-OH salt (poly[(9,9-bis(3′-(N-hydroxyethy-N,N-dimethyl amino) propyl)dibromide-2,7-fluorene)-alt-4,7-(thiophene)]); PFN-BT-OH salt (poly[(9,9-bis(3′-(N-hydroxyethyl-N,N-dimethylamino) propyl) dibromo-2,7-fluorene)-alt-4,7-(2,1,3-benzothiadiazole)]); and PFN-TBT-OH salt (poly- [(9,9-bis(3′-(N-hydroxyethyl,N,N-dimethy lamino) propyl) dibromide-2,7-fluorene)-alt-4,7-(dithienyl)-2,1,3 (benzothiadiazole)]).

The first category, containing PFN-T, PFN-BT, and PFN-TBT, contains hydrophilic amino parts and hydrophobic parts in the backbone. A small amount of acetic acid should be added to the polymer to improve its solubility in MeOH, leading to orthogonal solubility with the active layer. In our previous study, we discovered the acid additive in PFN enhanced the performance of the devices. However, this may deteriorate the ZnO layer because of its acidic nature [41]. Modifying the hydrophilic amino part by quaternization to increase solubility in MeOH is

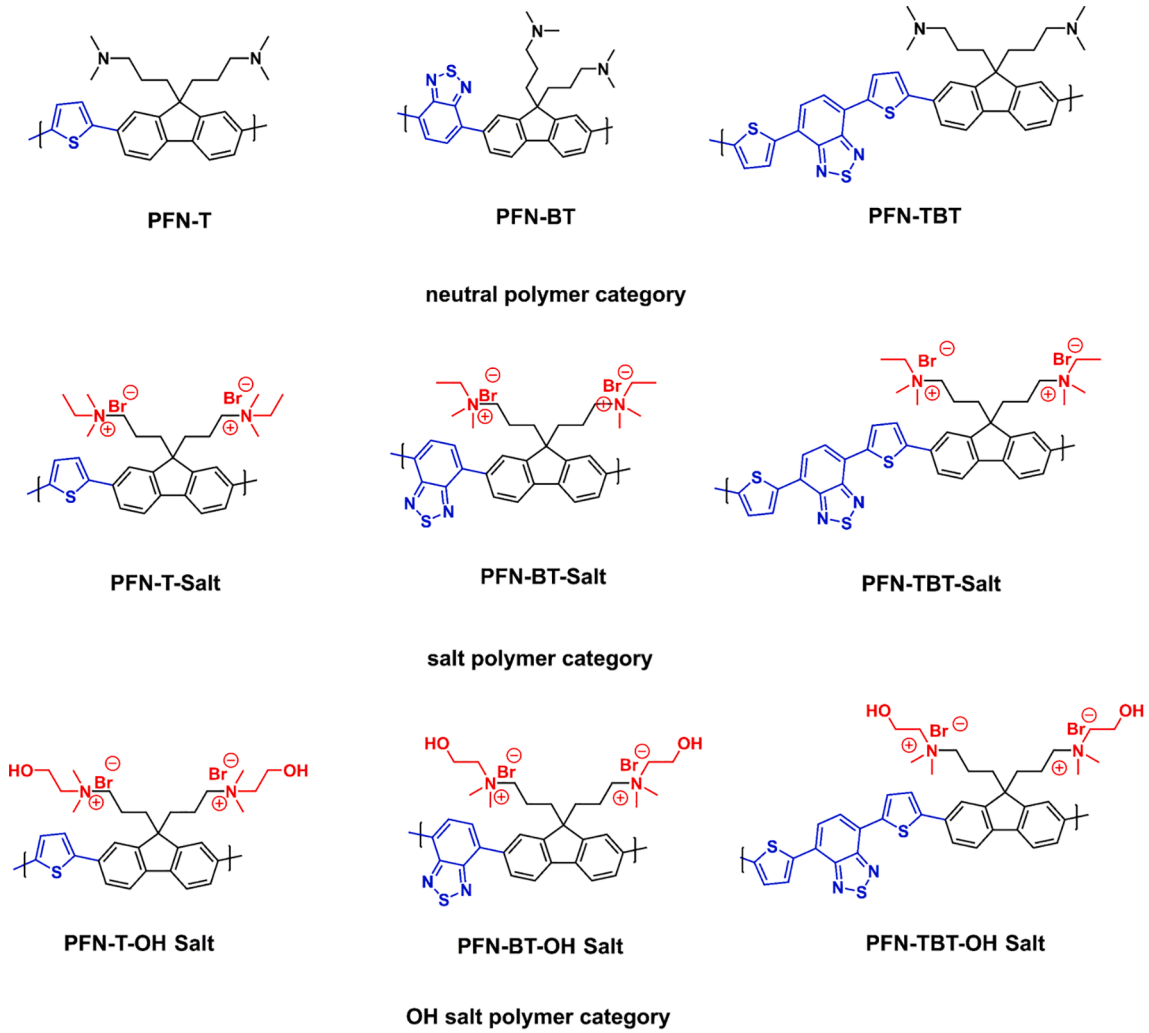

Fig. 1. Chemical structures of neutral, salt, and OH salt polymer categories.

required to overcome the ZnO layer deterioration. Two types of quaternarized agents were used: bromoethane and bromoethanol. In previous studies, organic electrolytes with hydroxyl groups were prepared and deposited as the interlayer for inverted PSCs [42,43]. Inspired by the excellent interface characteristics of hydroxyl groups, we focused on interface dipole modification by introducing a hydroxyl group and a quaternary ammonium bromide salt. The presence of a quaternary ammonium salt, which contains CPE, leads to a high J_{SC} in solar cells. The synergistic effect of the interlayer allows embedding in the ZnO layer. This is due to the formation of a favorable interface dipole between the ZnO and the quaternary ammonium salt layer. The electron collection ability from the active to the electron transport layer is improved by reducing the interface energy barrier [44-46].

Using the neutral polymer and polymer salt as the interlayer in the inverted device structure (ITO/ZnO/interlayer/PTB7-Th: $PC_{71}BM$/MoO_3/Ag), we found that CPEs with OH salt polymers offered the highest PCEs as compared to neutral polymer PCEs. The PCEs of the neutral polymer PSCs were 8.80%, 9.94%, and 9.43% for PFN-T, PFN-BT, and PFN-TBT, respectively. The PCEs of the PSCs in the polymer salt category were 9.43%, 9.87%, and 9.74% for PFN-T salt, PFN-BT salt, and PFN-TBT salt, respectively. Finally, for the polymer hydroxy salt, the PCEs of the PSCs were 9.85%, 10.6%, and 10.0% for PFN-T-OH, PFN-BT-OH, and PFN-TBT-OH salts, respectively. Introducing a quaternarized polymer between the ZnO and active layer could achieve excellent PCE values for the PSCs. Additionally, the PCE of devices with quaternarized OH salt reached 10.6% owing to the synergistic effect of hydrogen bonding between the ZnO layer and the hydroxyl group in the quaternary salt. Moreover, a robust intramolecular charge transfer occurred because of the improved electron affinity in the electron-withdrawing moiety of BT.

2. Result and discussion

2.1. Optical and electrochemical properties

We performed ultraviolet–visible (UV–Vis) spectroscopy to investigate the optical properties of the polymers. The polymer solutions were prepared by dissolution in methanol with a 6:1 M ratio of acetic acid to polymer. Fig. 2 shows the absorption spectra of the CPE-based polymer thin film, and its optical properties are listed in Table 1. The maximum absorption of the PFN-T film appeared at 430 nm (Fig. 2a), which is slightly blue-shifted as compared to the PFN-T salt (414 nm) and the PFN-T-OH salt (426 nm). A similar hypsochromic shift was caused by the sodium salt end group to produce a conformational change in thiophene, as studied by Holdcroft et al. [47] The salts are held closer to the thienyl ring and exhibit steric effects, and the interaction between the salt substituent and lone pair electrons on the sulfur atom plays a dominant role. Therefore, the adjacent thienyl rings twisted and shortened conjugation lengths [48].

As shown in Fig. 2b, PFN-BT showed two broad absorption bands at 322 and 446 nm, respectively. A band in the shorter wavelength region corresponds to the π–π* transition, and an extended wavelength region corresponds to the intramolecular charge transfer (ICT) absorption, which is characteristic of conjugated polymers with a donor–acceptor architecture. In the ICT region, the PFN-BT salt and PFN-BT-OH salt films showed absorption bands at 448 and 444 nm, respectively, which are nearly the same as the absorption maxima of PFN-BT. This is presumably because the terminal amino salt groups are unlikely to affect adjacent benzothiadiazole ring interactions in the film state [49]. The optimized molecular orbitals of PFN-BT (Figure S1b) showed no steric effect, as the dimethyl aminopropyl fluorene and benzothiazole were far from each other. The PFN-TBT film exhibited two absorption bands (Fig. 2c) at 395 and 565 nm, which correspond to the π–π* transition of the backbone and ICT absorption, respectively. The absorption spectra of the PFN-TBT salt and the PFN-TBT-OH salt showed the same features. The maximum ICT absorption wavelengths of the PFN-TBT salt and the

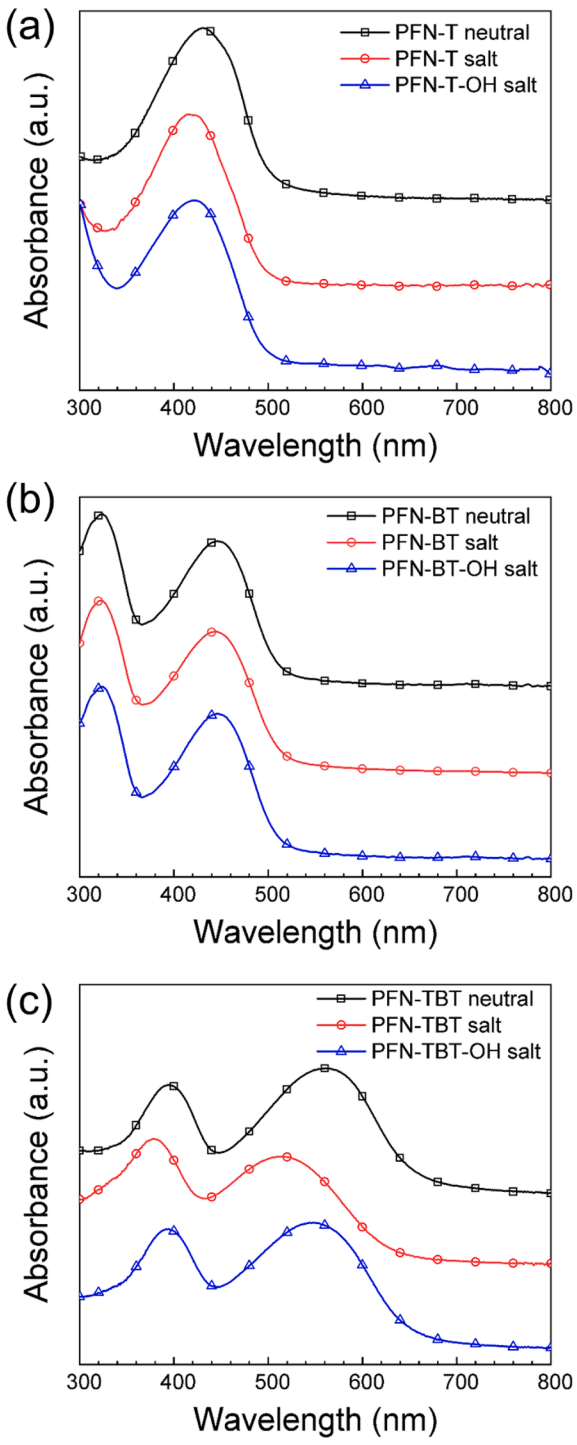

Fig. 2. UV–Vis spectra of (a) PFN-T series, (b) PFN-BT series, and (c) PFN-TBT series films.

PFN-TBT-OH salt were 512 and 549 nm, respectively, which were blue-shifted from those of PFN-TBT. This is possibly due to the steric hindrance between the thienyl segments in the TBT group. The FN group causes twisting of the adjacent thienyl rings and shortening of conjugation lengths. In the optimized computational structure of PFN-TBT (Figure S1c), the aminopropyl chain in the fluorene unit is settled in opposite directions to minimize electrostatic interactions. This effect bends the linkage between the two repeating units and produces a slight twist of the thiophene rings with the benzothiadiazole group [50].

The HOMO and LUMO energy levels of the polymers were

Table 1
Optical and electrochemical properties of CPE.

Sample	λ_{max}[a] (nm)	λ_{edge}[b] (nm)	HOMO[c] (eV)	LUMO[d] (eV)
PFN-T	430	502	−5.65	−3.32
PFN-T salt	414	493	–	–
PFN-T-OH salt	426	493	–	–
PFN-BT	322, 446	507	−5.57	−3.18
PFN-BT salt	322, 448	507	–	–
PFN-BT-OH salt	322, 444	507	–	–
PFN-TBT	395, 562	654	−5.66	−3.43
PFN-TBT salt	379, 512	628	–	–
PFN-TBT-OH	394, 549	646	–	–

a) maximum absorption.
b) optical bandgap obtained from the absorption edge.
c), d) obtained from oxidation and reduction onset potential of cyclic voltammogram.

determined from the oxidation and reduction onset potentials in cyclic voltammograms (CVs) (Figure S2). The CVs were calibrated using the ferrocene/ferrocenium (Fc/Fc^+) redox couple. Based on the onset reduction potential, the LUMO energy levels of PFN-T, PFN-BT, and PFN-TBT were −3.32 eV, −3.18 eV, and −3.43 eV, respectively. The HOMO energy levels of PFN-T, PFN-BT, and PFN-TBT were estimated to be −5.65. −5.57, and −5.66 eV, respectively. This result indicates that different electron-donating functional groups influence the HOMO level of the fluorene-based polymer, unlike the LUMO level, which is stabilized by introducing electron-withdrawing and electron-donating units on both sides of the FN.

2.2. Theoretical calculation of the polymers

The theoretical calculation was initially adopted to explore the electronic properties and provide preliminary insight into the geometric structures and dipolar properties of the interlayer materials. For simple computational calculations, the long side chains and polymer backbones were replaced with a methyl group and two repeating units. Density functional theory calculations were carried out using a B3LYP/6-31G(d) basis set based on the Gaussian suite of programs (Gaussian 09) [51]. The optimized geometries of the CPE interlayer materials with dihedral angles and dipole moments are depicted in Figure S3. Dihedral angles are defined as the 180° torsional angle deviation between the adjacent fluorene units surrounding the connecting bond. A small dihedral angle (i.e., planar structure) promotes delocalization of the π-electron system. Similarly, the bond length alternation parameter provides a quantitative measure of the homogeneous distribution of π electrons over the bonds (Peierls distortion) by comparing the consecutive bond lengths along the chain. Enhancing the electronic delocalization tends to equalize the bond lengths, reducing the bond length alternation [52].

The dihedral angles between the dimethylamino fluorene and the thiophene moiety in PFN-T were − 27.40° and 24.79°, respectively. The preferred conformation for thienyl rings is to be oriented anti, which minimizes the effect of steric hindrance [48]. The dihedral angles between the dimethyl amino fluorene and the benzothiadiazole moiety are − 37.06° and − 36.97°, suggesting that a strong steric hindrance effect occurs between the fluorene and BT moieties, adopting a nonplanar configuration, as depicted in (Figure S1b) [53]. PFN-TBT showed the most planar geometry with dihedral angles of − 24.42° and 23.93°. The thiophene link between the FN segment and benzothiadiazole caused conformational effects. The structural variation resulted in a distinctly different dihedral angle between the thiophene unit and flanked benzene in the fluorene moiety.

The one-thiophene bridge in PFN-T has larger dihedral angles than in the two-thiophene bridge in PFN-TBT. This thiophene bridge makes the backbone of PFN-TBT more flexible and increases the distance between the two polar groups, weakening the repulsion to a certain degree to obtain the smaller dihedral angles of PFN-TBT. The largest dihedral angle was observed for PFN-BT due to the interchain interaction. A reasonable conformation for fluorene-based polymers has an all-trans or near-trans conformation dihedral angle, as the fully trans conformation is energetically unfavorable (as it is sterically hindered) [54].

The calculated dipole moments of the polymers are shown in Figure S1. The trend was estimated as follows: PFN-BT (3.45 D) > PFN-TBT (2.08 D) > PFN-T (1.60 D). As shown in Figure S1, the thiophene (T) bridge in PFN-TBT and PFN-T caused small permanent dipoles. Notably, the PFN-BT has a benzothiadiazole group in the backbone at the opposite side of the polar group, which helps acquire a more decisive dipole moment (3.45 D). The dipole moment in this calculated result corresponds to the dihedral angle. Seo et al. [55] reported that a larger interfacial dipole on the CPE could arise from the higher permanent dipole moment. The primary requirement of an interlayer is its ability to produce large interfacial dipoles that induce a vacuum-level shift to modify the electrode work function [56].

The frontier molecular orbitals of the two repeating units with theoretical HOMO/LUMO energy levels are shown in Figure S3. The calculated HOMO/LUMO energy levels exhibited similar trends in the UV–Vis and CV experiments. However, the orbital character of the CPE interlayer dimers showed different delocalized electrons. In particular, the HOMO energy levels are accessed when thiophene and benzothiadiazole are incorporated into the polymer backbone in PFN-T, PFN-BT, and PFN-TBT. Additionally, at the HOMO level, electrons are delocalized along the chain direction, whereas their localization takes place in the electron-withdrawing unit at the LUMO level for PFN-BT and PFN-TBT.

2.3. Optical simulation characteristic of the devices using transfer matrix formalism

To confirm the role of the interlayer, an optical model for CPE-based devices was carried out using transfer matrix formalism (TMF). This provides a guideline for predicting the optimized device architecture. The optical constants, refractive index (n), and extinction coefficient (k) values of the selected CPE, PTB7-Th:$PC_{71}BM$, were determined using ellipsometry spectroscopy, and those of ITO, ZnO, MoO_3, and Ag were obtained from previous literature [57-60]. In this study, a MATLAB script, developed by the McGhee group, was used for transfer matrix optical modeling [57]. The absorption distribution over the film thickness was calculated in the wavelength range of 300–800 nm. Multiplying with the AM 1.5 sun spectrum and integrating over the film thickness resulted in optical electric field profiles corresponding to various position wavelengths, as depicted in Fig. 3 [61]. The device with an interlayer showed prominent electrical field peaks located inside the active layer for the four incident lights from 350 to 650 nm. This simulation indicates that the interlayer structures cause a slight change in the optical electric field (OEF) distribution. As depicted in Fig. 3a, c, e, and g, the device with pristine ZnO showed the lowest OEF intensity compared with the devices with interlayers, while the device based on PFN-BT exhibited the highest OEF intensity. The field intensity over the entire wavelength range of 300–1100 nm was mapped to obtain the OEF distribution details. Fig. 3b, d, f, and h show the normalized field intensity versus distance at different incident light wavelengths for each layer in the solar cell. Visibly, the 350–650 nm wavelength region shows a slight influence of thin-film interference, with higher OEF developing from constructive interference. Although very thin, ±5 nm CPE layers exist, and the alteration in the OEF distribution spectra indicates that the optical effect of the CPE backbone is responsible for the modifications in the interlayer active layer region in the device. The OEF spectra of devices with PFN-BT show the highest intensity, which is strongly influenced by the parasitic absorption of CPEs and the constructive and destructive interference between incident and reflected light [59].

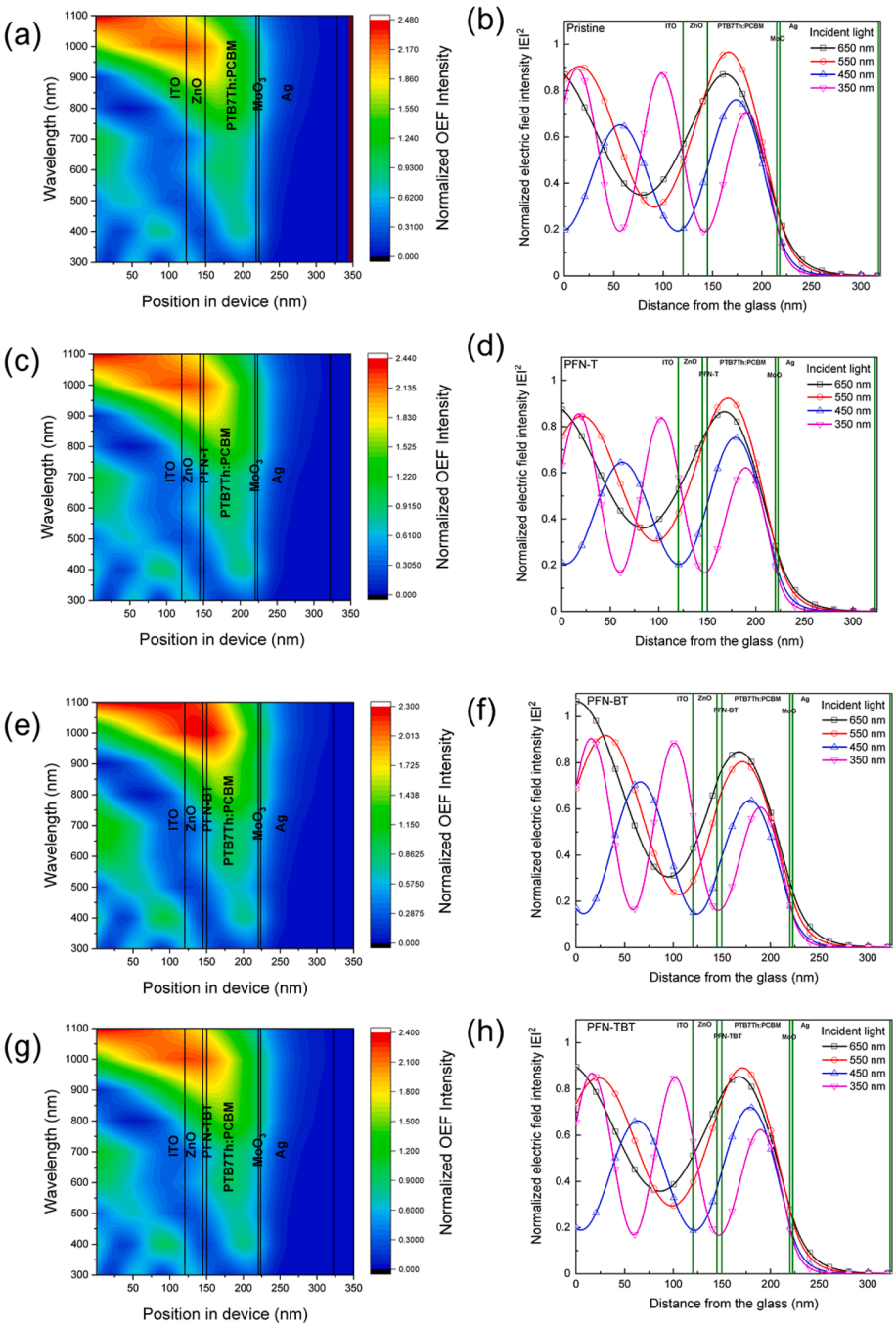

Fig. 3. Optical electric field intensity of (a, b) pristine, (c, d) PFN-T, (e, f) PFN-BT, and (g, h) PFN-TBT by TMF optical simulation.

2.4. Investigation of the CPE-covered ZnO surface

Water contact angle characterization is used to provide intuitive information about the surface component wettability. The surface properties of the ZnO/CPEs were investigated using water contact angle measurements (Figure S4). The water contact angle of the ZnO/neutral polymer category was higher than that of both the ZnO/salt polymers and the OH salt polymers owing to the hydrophobic properties of the neutral polymer category. The water contact angles of the ZnO surface with PFN-T, PFN-BT, and PFN-TBT were 50.9°, 51.3°, and 51.9°, respectively, all of which were higher than the pristine ZnO value (28.6°). In Figure S5, quaternarized CPEs showed a low water contact angle due to increased polymer salt hydrophilicity and hydrogen bond formation of the polymer-OH salt. The values for PFN-T salt, PFN-BT salt, and PFN-TBT salt were 42.3°, 37.3°, and 48.7°, respectively, and those for PFN-T-OH salt, PFN-BT-OH salt, and PFN-TBT-OH salt were 31.3°, 32.8°, and 44.6°, respectively. In general, a small water contact angle indicates a suitable wetting property and is advantageous for using CPEs interlayers in solar cells. The smaller contact angle was attribute to interfacial modification with salt and OH-salt CPEs layer. Thus, the compatibilities between ZnO and the active layer with ZnO/CPEs were better. The surface contact angle measurement shows that the self-assembly CPEs layer has a better wettability than that of the spin-coated film, which means that there are more side chains of self-assembly PFN outward away from the substrate [62].

Kelvin probe microscopy measurements were performed to investigate the influence of CPEs on the ZnO work function. Fig. 4 shows the work function (WF) of ZnO with neutral, salt, and OH salt polymer

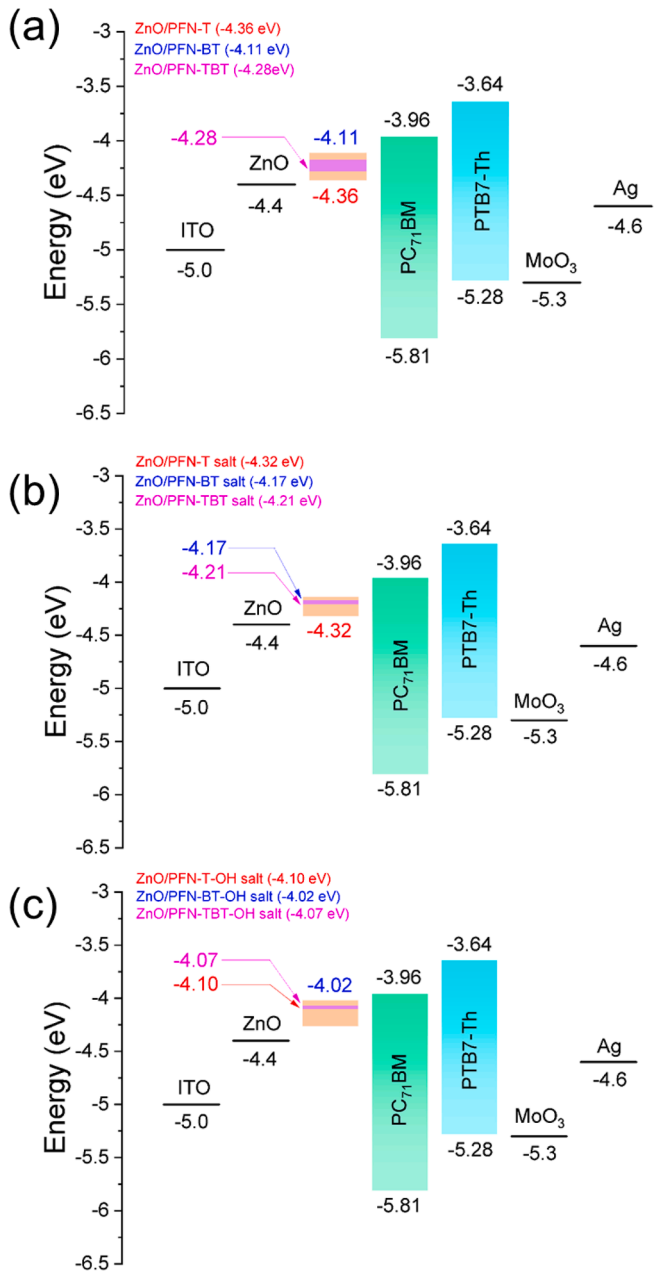

Fig. 4. Energy level diagrams of (a) ZnO/neutral, (b) ZnO/salt, and (c) ZnO/OH salt polymer categories.

categories. The WF values of ZnO with neutral PFN-T, PFN-BT, and PFN-TBT were − 4.36, −4.11, and − 4.28 eV, respectively. The WF values based on PFN-T salt, PFN-BT salt, and PFN-TBT salt were − 4.32, −4.17, and − 4.21 eV, respectively. The WF values based on PFN-T-OH salt, PFN-BT-OH salt, and PFN-TBT-OH salt were − 4.10, −4.02, and − 4.07 eV, respectively. The WF values for ZnO with interlayers were higher than those of ZnO without an interlayer (−4.4 eV). The mechanism resulting in PCE improvement is attributed to the WF change at the ZnO surface by interface dipole formation [63], which can be tuned by introducing an interlayer, that is, transition from a Schottky to an Ohmic contact. Thus, the reduced barrier height at the ZnO surface might improve the charge collection capability [36,64,65].

For polymer salts, a higher interface dipole can be expected because the polymer salt dipole moment magnitude may be greater than that of neutral polymers. The neutral polymer is soluble in alcohol in the presence of a small amount of acetic acid because of the weak interaction between the nitrogen atoms in the side chain and the acetic acid. Compared with polymer salts, it dissolves easily in polar solvents. Neutral amine groups in neutral polymers are primarily physisorbed onto the ZnO surface [66,67]. The WF reduction and energy level adjustment are due to the amine CPE intrinsic molecular dipole (μMD) synergistic effect acting perpendicular to the surface and to the interfacial dipole (μID) formed at the interface of the modifier molecules and the electrode surface. The contribution of the μID is attributed to partial electron transfer from the amine-containing molecules to the electrode surface [62,66,68,69]. The magnitude of the dipole moment based on the OH salt polymer category is higher than that of the polymer salts due to polar –OH groups, which generate a synergistic effect on the dipole moment magnitude. Thus, the magnitude of the interface dipole moment for the OH salt polymer category > the salt polymer category > the neutral polymer category. The trend for J_{sc} is the trend of the WF. Generally, the WF difference in the charge transporting layer is not the main factor affecting the built-in potential and V_{OC} Fermi-level pinning [70].

Park et al. studied the spontaneous organization of side chains on CPE [71]. Based on our previous study, we discovered that the CPE quaternarized side chain affects the WF and wetting ability due to the spontaneous arrangement of the side chain [72,73]. In the stacking device architecture, upon introducing an interlayer between ZnO and the active layer, the ionic groups on the CPE backbone were directed away from the active layer surface. Simultaneously, the side chains pointed toward the ZnO layer owing to the spontaneous reorganization. The increased number of accumulated ionic groups on the CPE led to an Ohmic contact and increased wettability of the active layer.

2.5. Photovoltaic properties

To investigate the photovoltaic properties of the device with CPE interlayers, we constructed and tested inverted-type PSCs with an ITO/ZnO/interlayer/PTB7-Th:$PC_{71}BM$/MoO_3/Ag structure (Fig. 5a). The current density–voltage ($J-V$) curves of the PSCs with the PFN CPE interlayer under illumination (inset: under dark conditions) are shown in Fig. 5b–c. Additionally, the photovoltaic parameters are summarized in Table 2. Devices based on the PFN interlayer showed higher PCEs than those based on pristine ZnO. This indicates that PFN derivatives are potential materials for interfacial modification to improve device performance. The PCEs of the PSCs with the neutral categories of PFN-T, PFN-BT, and PFN-TBT were 8.80%, 9.94%, and 9.43%, respectively. The relative improvements in the PCE based on PFN-BT and PFN-TBT were 13.7% and 7.89%, respectively, upon comparison with the pristine ZnO-based device. However, the PCE of the device based on PFN-T was almost identical to that of the device based on pristine ZnO. The improvement in the performance of neutral PFN category devices mainly arises from the simultaneous enhancements of J_{SC} and FF.

The devices based on the salt polymer category exhibited improved performance compared with the device based on pristine ZnO. The PCEs of the devices based on PFN-T salt, PFN-BT salt, and PFN-TBT salt were 9.43%, 9.87%, and 9.74%, respectively. The highest PCE was observed for the device with PFN-BT salt. The PCE improvement of the devices based on PFN-T salt, PFN-BT salt, and PFN-TBT salt were 7.89%, 12.93%, and 11.4%, respectively, compared with those of pristine ZnO devices. The PCEs of the devices based on PFN-T-OH salt, PFN-BT-OH salt, and PFN-TBT-OH salt were 9.85%, 10.6%, and 10.0%, respectively. The devices based upon the OH salt polymer category showed significantly improved PCEs. Essentially, the side chain functionality helped increase device performance. Note that the calculated J_{SC} values obtained from the incident photon-to-current efficiency (IPCE) curves (Figure S6) were in good agreement with the values obtained under 1.0 sun illumination.

The PCE of the devices based on the neutral polymer category was in the order PFN-BT > PFN-TBT > PFN-T. The result agreed well with the calculated dipole. The synergistic effect from the side chain and different

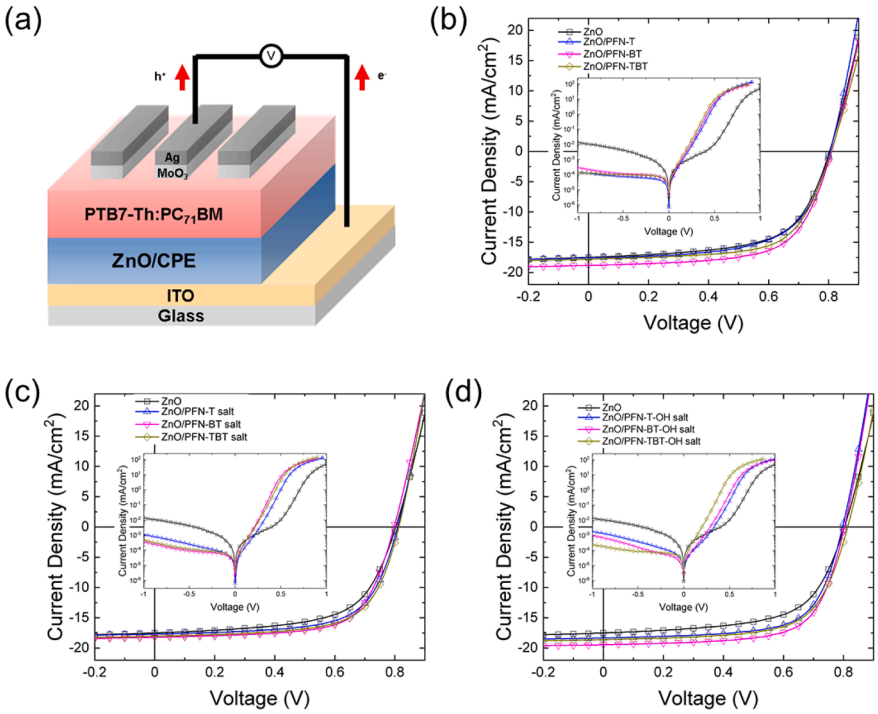

Fig. 5. (a) Device architecture, *J-V* curves of PSCs based on (b) neutral, (c) salt, and (d) OH salt polymer category as the interlayer.

backbone structures influence the interfacial dipole magnitude and direction. PFN-T exhibited the lowest PCE among the neutral polymers owing to the lowest interfacial dipole moment and optical effect. The thienyl rings were twisted and had shorter conjugation lengths [47]. The comprehensive and planar π-conjugated system in PFN-TBT affects WF and charge mobility. Thus, PFN-TBT showed a higher PCE than PFN-T. The benzothiadiazole in PFN-BT enhanced electron mobility due to the high content of electron-deficient BT units. This was probably due to the non-covalent attractive interactions among S, C, H (in thiophene) and nitrogen (in BT), which minimized the torsional angle [48]. A smaller torsional angle maximizes the polymer planarity chain, resulting in efficient charge transport. Thus, PFN-BT showed better performance than that of PFN-T and PFN-TBT. The PCE of the devices based on the salt polymer and OH salt polymer categories follows the trend of the PCEs in the neutral polymer category.

Devices without an interlayer exhibited the lowest performance, where the combination of low V_{OC}, J_{SC}, and *FF* resulted in an 8.74% PCE. The low performance of the device based on pristine ZnO among the devices can be explained by a mismatch of the WF between the active and electrode layers and a low charge extraction due to high contact resistance [36,64,74]. A noticeable correlation was found between the CPE functionality and the PCEs of the devices. Devices based on salt polymers as the interlayer exhibited improved PCEs than those of devices based on neutral polymers. Notably, the PCE improvement mainly resulted from the J_{SC} enhancement [31,75-77]. The work function data agree well with the trend of J_{SC} data. (Figure S5a).

The electron mobilities of the devices [ITO/ZnO with or without interlayer/$PC_{71}BM$ (60 nm)/Al (100 nm)] were studied to understand the effect of the interlayer on the device electron transport properties. The Mott–Gurney law was adopted to calculate the electron mobility [78]. We can easily notice that the electron mobilities of the devices with PFN as the interlayer are higher than those of the device based on pristine ZnO (2.64×10^{-3} cm^{-2} V^{-1} s^{-1}). The electron mobilities of the devices with PFN-T, PFN-BT, and PFN-TBT were 2.76×10^{-3}, 4.13×10^{-3}, and 3.41×10^{-3} cm^{-2} V^{-1} s^{-1}, respectively. The calculated electron mobilities of the devices based on PFN-T salt, PFN-BT salt, and PFN-TBT salt were 3.01×10^{-3}, 3.87×10^{-3}, and 3.71×10^{-3} cm^{-2} V^{-1} s^{-1}, respectively. The electron mobilities of the devices based on PFN-T-OH salt, PFN-BT-OH salt, and PFN-TBT-OH salt were 4.27×10^{-3}, 4.66×10^{-3}, and 4.3×10^{-3} cm^{-2} V^{-1} s^{-1}, respectively. The higher electron mobilities of the devices based on salt polymer and OH salt polymer categories were higher than those of the devices based on the neutral polymer category, which can be explained by their better cathode modification capability, and the larger electron mobilities of the interlayer-based devices can be ascribed to the J_{SC} data trend of the PSCs.

As summarized in Table 2, the series resistance (R_s) was determined from the inverse slope near the high current regime in the current density–voltage curves obtained under 1.0 sun conditions. Under the illuminated condition, the R_s values of the devices with PFN-T, PFN-BT, and PFN-TBT were 4.40, 4.05, and 4.29 Ω cm^2, respectively. The R_s values for devices based on PFN-T salt, PFN-BT salt, and PFN-TBT salt were 4.34, 4.09, and 4.17 Ω cm^2, respectively. The R_s values for devices based on PFN-T-OH salt, PFN-BT-OH salt, and PFN-TBT-OH salt were 4.04, 3.76, and 3.98 Ω cm^2, respectively. The R_s value for pristine ZnO was 5.26 Ω cm^2. Evidently, the R_s values of the devices have strong correlations with the trend in the PSC polymer photovoltaic properties (Figure S5a).

This R_s could be attributed to the Ohmic loss of the entire device, including bulk and contact resistance. Therefore, R_s was affected by the resistivity of the pristine ZnO, the ZnO/interlayer, and factors such as the contact resistance between different layers [79]. The excellent FF can be further verified by the R_s and the shunt resistance (R_{sh}) calculated from the $J-V$ curves. The smallest R_s and the largest R_{sh} values indicate that the charge carrier transport and collection ability are enhanced by using ZnO/CPEs, resulting in an increase in FF and PCE [80]. R_{sh} represents the current leakage from the cell edges and from the device. Several groups have reported that metal atoms, during thermal evaporation, can damage the active layer surface and diffuse inside the blend. Metal atoms are active centers for carrier recombination; hence, the current loss increases as reflected by a decrease in R_{sh} [81]. The R_{sh} value was obtained from the $J-V$ curve under illumination. The R_s values of the devices based on PFN-T, PFN-BT, and PFN-TBT were 578, 710, and 714 kΩ cm^2, respectively. For the devices based on PFN-T salt,

Table 2
Performance data of the PSCs with CPEs with the highest PCE. The averages of 20 devices are summarized in parentheses.

	J_{sc}[a] (mA/cm^2)	$J_{sc,\ cal}^{b}$ (mA/cm^2)	V_{oc} (V)	FF (%)	PCE (%)	R_s^b (Ω cm^2)	R_{sh}^c (Ω cm^2)
ZnO	17.5 (17.4)	17.5	0.80 (0.80)	62.2 (62.1)	8.74 (8.71)	5.26	552
ZnO/ PFN-T	17.6 (17.5 ± 0.09)	17.6	0.81 (0.80 ± 0.09)	62.3 (61.6 ± 0.73)	8.80 (8.69 ± 0.13)	4.40	578
ZnO/ PFN-BT	18.8 (18.7 ± 0.11)	18.8	0.81 (0.81 ± 0.00)	65.1 (63.9 ± 1.35)	9.94 (9.78 ± 0.23)	4.05	710
ZnO/ PFN-TBT	17.8 (17.7 ± 0.10)	17.9	0.81 (0.81 ± 0.00)	65.4 (64.7 ± 0.73)	9.43 (9.32 ± 0.15)	4.29	714
ZnO/ PFN-T salt	17.7 (17.6 ± 0.02)	17.7	0.81 (0.80 ± 0.00)	66.3 (65.4 ± 0.73)	9.43 (9.28 ± 0.14)	4.34	792
ZnO/ PFN-BT salt	18.2 (18.1 ± 0.13)	18.2	0.80 (0.80)	67.4 (66.7 ± 0.99)	9.87 (9.65 ± 0.28)	4.09	899
ZnO/ PFN-TBT salt	18.0 (17.90 ± 0.09)	18.1	0.81 (0.81 ± 0.00)	66.7 (65.6 ± 1.08)	9.74 (9.64 ± 0.11)	4.17	814
ZnO/ PFN-T-OH salt	18.3 (18.2 ± 0.04)	18.9	0.80 (0.80 ± 0.00)	67.0 (66.4 ± 0.13)	9.85 (9.79 ± 0.22)	4.04	911
ZnO/ PFN-BT-OH salt	19.4 s(19.30 ± 0.09)	19.5	0.80 (0.80 ± 0.00)	68.4 (67.3 ± 1.39)	10.6 (10.5 ± 0.23)	3.76	916
ZnO/ PFN-TBT-OH salt	18.6 (18.5 ± 0.08)	19.2	0.81 (0.80 ± 0.00)	66.4 (66.3 ± 0.93)	10.0 (9.96 ± 0.15)	3.98	905

[a] Calculated from the IPCE curves, [b] series, and [c] shunt resistance under illumination.

PFN-BT salt, and PFN-TBT salt, the R_{sh} values were 505, 792, 899, and 814 kΩ cm^2, respectively. The R_{sh} values for the device based on PFN-T-OH salt, PFN-BT-OH salt, and PFN-TBT-OH salt were 911, 916, and 905 kΩ cm^2, respectively, which are higher than those of devices with pristine ZnO (552 kΩ cm^2). This R_{sh} is consistent with the device ***FF*** values, suggesting that the interlayer helps increase the R_{sh} by eliminating short circuits between the contacts, which contributes to increased device efficiency. However, the increased shunt resistance may not be the sole reason for the increased device efficiency. The incorporation of CPE as an interlayer in the devices can also influence their electrical characteristics. The R_{sh} of the CPE-based device increases in the order of neutral < salt < OH salt polymer category. Additionally, the R_{sh} tendency increases coherently with ***FF***, indicating improved device characteristics (Figure S5b). Electrical properties, such as low series resistance and high shunt resistance, of the devices based on neutral polymer, salt polymer, and OH salt polymer categories, are responsible for the increased ***FF***.

We evaluated the relationship between photocurrent density (J_{ph}) and effective voltage (V_{eff}) to understand the charge transport and collection properties of the devices with and without an interlayer. Here, J_{ph} and V_{eff} were defined by J_L (measured current density under illumination) – J_D (measured current density in dark condition) and V_0 (voltage at $J_{ph} = 0$) – V_a (applied voltage), respectively. As shown in

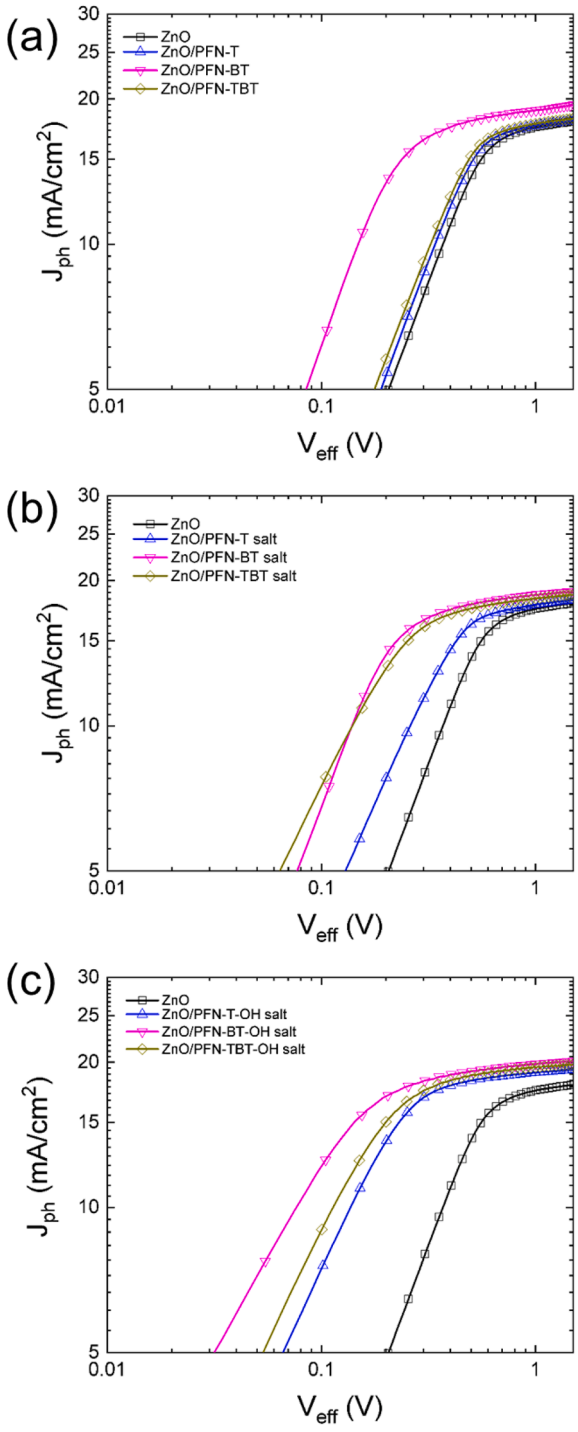

Fig. 6. Photocurrent (J_{ph}) density vs. effective voltage (V_{eff}) of (a) neutral, (b) salt, and (c) OH salt polymer categories.

Fig. 6, the log (J_{ph}) vs. log (V_{eff}) showed a linear relationship with a low V_{eff} range and began saturating at a high V_{eff} region. The V_{eff} values of the devices in the saturated photocurrent regime (V_{sat}) based on PFN-T, PFN-BT, and PFN-TBT were 0.53, 0.22, and 0.53 V, respectively, which were smaller than those of the pristine ZnO-based device (0.56 V). The V_{sat} values of the devices based on PFN-T salt, PFN-BT salt, and PFN-TBT salt were 0.44, 0.33, and 0.26 V, respectively. Additionally, the V_{sat} values of the devices with PFN-T-OH salt, PFN-BT-OH salt, and PFN-TBT-OH salt were 0.27, 0.18, and 0.24 V, respectively. Notably, the magnitude of V_{sat} is in the order of neutral polymer > salt polymer > OH salt polymer categories. This trend corresponds with the changes in J_{SC}

and PCE of the devices because a smaller V_{sat} indicates a faster transition from the space-charge-limited regime to the saturation regime. In other words, there is a low V_{sat} energy barrier in the devices.

The saturation current density (J_{sat}) can be correlated with the maximum exciton generation rate (G_{max}), the exciton dissociation probability, the carrier transport, and the collection probability at high V_{eff}. G_{max} depends on the absorption of light on the active layer and was determined by $J_{ph}/q{\cdot}L$, where q is the electron charge and L is the thickness of the active layer [82]. Additionally, the carrier transporting and collecting probability current saturation point was estimated using J_{ph}/J_{sat} at any V_{eff}. The G_{max} value under the J_{sat} condition of the devices based on pristine ZnO was 1.57×10^{28} m^{-3} s^{-1} and the values for the ZnO/PFN-T, ZnO/PFN-BT, and ZnO/PFN-TBT devices were 1.58×10^{28}, 1.68×10^{28}, and 1.61×10^{28} m^{-3} s^{-1}, respectively. The PFN-T salt, PFN-BT salt, and PFN-TBT salt derivatives-based devices exhibited G_{max} values of 1.58×10^{28}, 1.62×10^{28}, and 1.59×10^{28} m^{-3} s^{-1}, respectively. The G_{max} values for PFN-T-OH salt, PFN-BT-OH salt, and PFN-TBT-OH salt-based devices were 1.64×10^{28}, 1.69×10^{28}, and 1.73×10^{28} m^{-3} s^{-1}, respectively. No significant change was observed in G_{max} as it is dependent on the active layer absorbance. J_{sat} is limited by carrier transport and collection upon dissociation of photo-generated excitons into free charge carriers at high V_{eff} [41]. The point of V_{eff} reached at saturated photocurrent, G_{max}, and the carrier transporting and collecting probability have a strong correlation with the trend in J_{SC} values. These values reveal that the CPEs exhibited reduced charge recombination and increased charge collection capability at the cathode layer interfaces.

The dependence of J_{SC} and V_{OC} on light intensity (P_{light}) was measured to investigate charge carrier recombination, which is shown via the J_{SC} vs. P_{light} and the V_{OC} vs. P_{light} curves and their slopes. The relationship between J_{SC} and P_{light} is explained by the equation $J_{SC} \propto (P_{light})^{\alpha}$, where the value of α is unity when the bimolecular charge recombination is negligible [83]. As shown in Fig. 7, the α value of the device without the interlayer was 0.960. The α values of the devices with PFN-T, PFN-BT, and PFN-TBT were 0.964, 0.967, and 0.972, respectively. The α values for devices based on PFN-T salt, PFN-BT salt, and PFN-TBT salt were 0.975, 0.957, and 1.029, respectively. The devices based on PFN-T-OH salt, PFN-BT-OH salt, and PFN-TBT-OH salt showed α values of 0.966, 0.960, and 0.974, respectively. According to the results, devices that exhibit bimolecular recombination are suppressed in PSCs with CPE interlayers. In BHJ-type solar cells, bimolecular recombination occurs mainly at the donor–acceptor interfaces of the active layer and the interlayers. Devices suppress recombination because of the decreased space charge at the interfaces [84].

The relationship between V_{oc} and intensity (P_{light}) is explained by $V_{oc} \mu s k T/q \, ln(P_{light})$, where k, T, q and P_{light} are the Boltzmann constant, temperature in Kelvin, electron charge, and illumination intensity, respectively. The slope, s, of the V_{oc} vs. P_{light} curve provides information about trap-assisted recombination. The slope has a value of 1 when the band-to-band (Langevin) recombination is superior to the trap-assisted recombination. If devices have only trap-assisted recombination, the s value is 2. The slopes of the V_{oc} vs. P_{light} curves with and without the PFN of the CPE-based devices are shown in Figure S7. For neutral polymers, devices without the PFN interlayer exhibited a s value of 1.46. The s values of the devices based on PFN-T, PFN-BT, and PFN-TBT were 1.43, 1.25, and 1.36, respectively. The s values for devices based on PFN-T salt, PFN-BT salt, and PFN-TBT salt were 1.35, 1.87, and 1.27, respectively. The devices based on PFN-T-OH salt, PFN-BT-OH salt, and PFN-TBT-OH salt have s values of 1.22, 1.19, and 1.19, respectively. These results prove the effectiveness of CPEs on reducing the numbers of traps. The changes in the s values of devices correspond with the trend shown by the PCEs of PSCs and follow the FF trend.

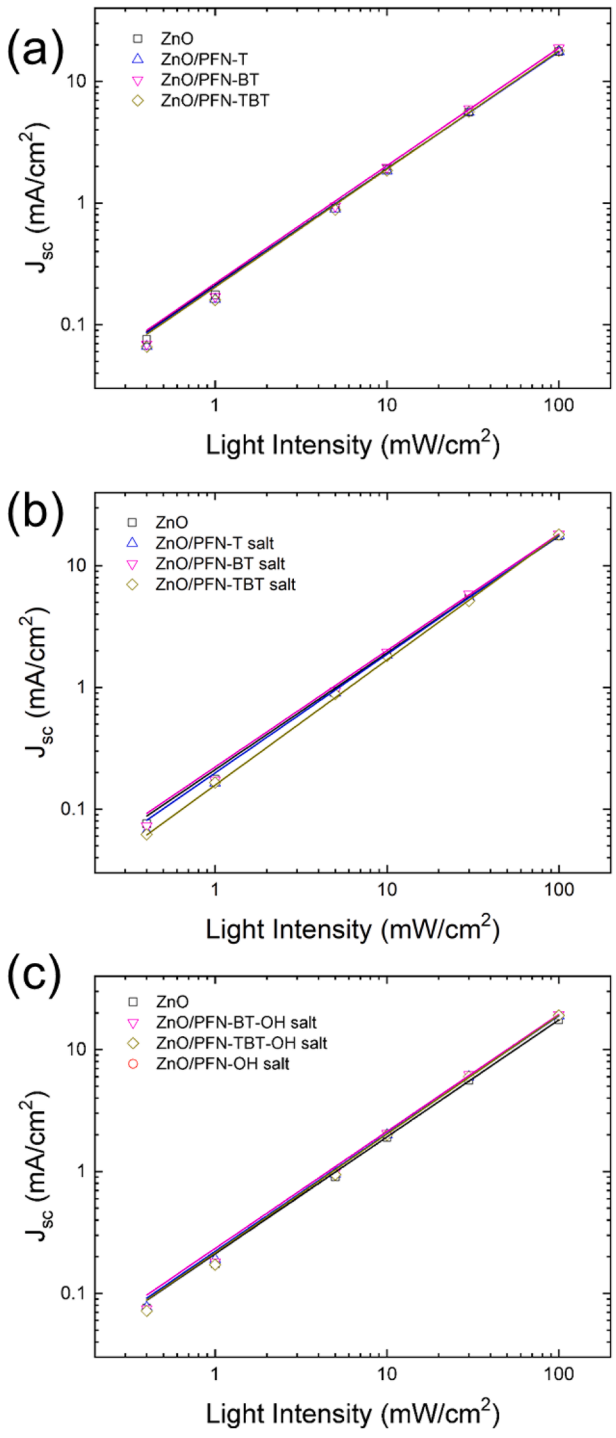

Fig. 7. Dependence of J_{SC} on light intensity of (a) neutral, (b) salt, and (c) OH salt polymer categories.

2.6. Electronic impedance spectroscopy (EIS) of PSCs

Electronic impedance spectroscopy (EIS) was performed to investigate the carrier transport and recombination mechanisms. As shown in Fig. 8, the data were fitted to estimate the recombination resistance (R_{rec}). Efficient charge collection was implied by transport resistance, which is smaller than R_{rec}. The EIS spectra followed the Gerischer impedance model for intense recombination. The absence of a transmission line indicates that the devices experienced strong recombination. In the Nyquist plots in Fig. 8, the respective electrochemical steps with different time constants are represented by semicircles. The

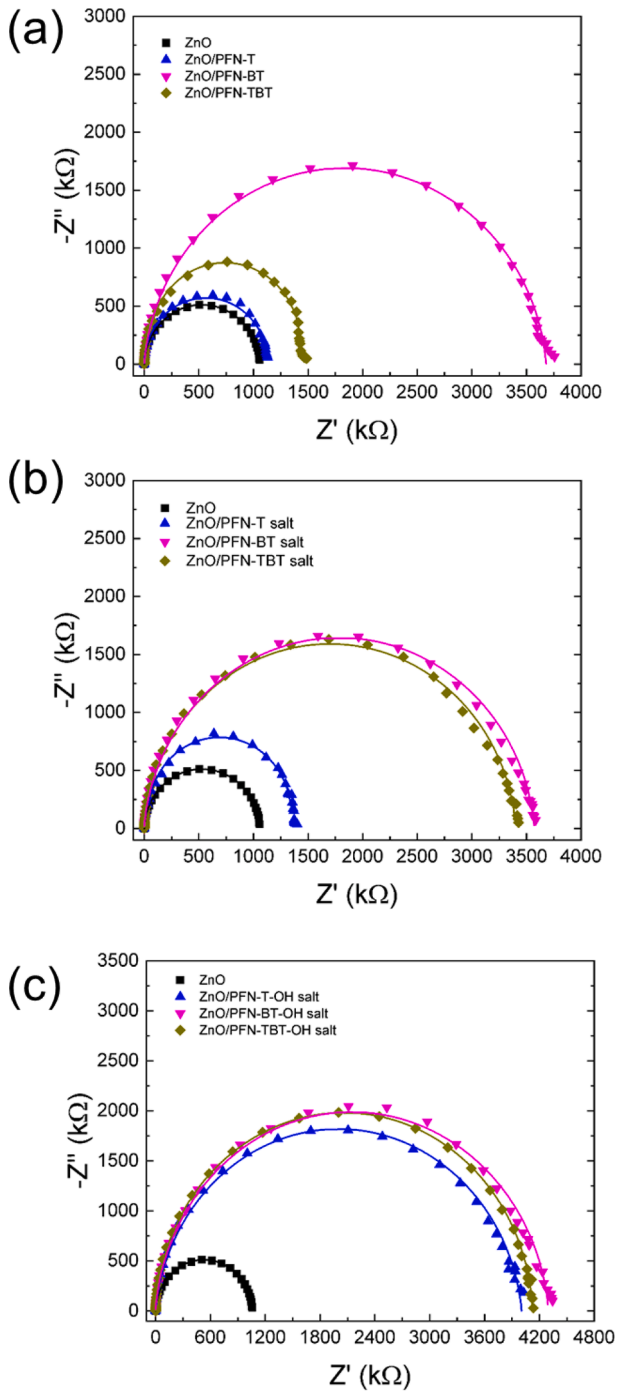

Fig. 8. Impedance spectra of (a) neutral, (b) salt, and (c) OH salt polymer category.

distance between the intercepts at the real axis corresponds to the charge-transfer resistance of the device [85-92]. The larger the EIS semicircle, the greater the R_{rec}. The higher R_{rec} values are related to the charge extraction capability at the ZnO interfaces. The R_{rec} values for devices based on PFN-T, PFN-BT, and PFN-TBT were 1133, 1326, and 1450 kΩ, respectively. The R_{rec} values for devices based on PFN-T salt, PFN-BT salt, and PFN-TBT salt were 2081, 3585, and 2582 kΩ, respectively. The R_{rec} values for devices based on PFN-T-OH salt, PFN-BT-OH salt, and PFN-TBT-OH salt were 3899, 4620, and 3694 kΩ, respectively. The semicircle size increased, leading to an increase in R_{rec}. The R_{rec} magnitude of the device was in the order: neutral polymer < salt polymer < OH salt polymer categories, indicating that the lowest reduced interfacial recombination corroborates with the R_{sh} and FF of PSCs. Additionally, the EIS results are consistent with the relationship between the V_{oc} and intensity (P_{light}) of the PSCs.

3. Conclusion

We synthesized and characterized a series of CPEs divided into three categories: neutral polymer, salt polymer, and OH salt polymer. Each category contained three different backbones (T, BT, TBT). The CPEs were introduced as interlayers in inverted PSCs with an ITO/ZnO/CPE/PTB7-Th: $PC_{71}BM/MoO_3$/Ag structure. The highest PCE, 10.6%, was achieved with the PFN-BT-OH salt. Combined with surface contact angle measurement, optical simulation, and photovoltaic characterization of solar cells, we found that the PCEs of the CPE-based devices depended on the backbone structure and the side chain functionality. Different backbone structures resulted in varied molecular dipole moments, and the side chain functionality induced a larger interface dipole and spontaneous organization. This synergistic effect of the backbone and the side chain functionality, and J_{SC} improvement greatly contributed to PCE enhancement due to the energy offset reduction at the cathode interface.

Declaration of Competing Interest

The authors declare that they have no known competing financial interests or personal relationships that could have appeared to influence the work reported in this paper.

Acknowledgments

This research was supported by the Korea Institute of Energy Technology Evaluation and Planning (20182010106360A) and the National Research Foundation (NRF) of Korea under the program number 2019R1A2C1002585.

Appendix A. Supplementary data

Supplementary data to this article can be found online at https://doi.org/10.1016/j.cej.2021.129895.

References

[1] X. Li, X. Liu, W. Zhang, H.Q. Wang, J. Fang, Chem. Mater. 29 (2017) 4176.
[2] Z. Wu, C. Sun, S. Dong, X.F. Jiang, S. Wu, H. Wu, H.L. Yip, F. Huang, Y. Cao, J. Am. Chem. Soc. 2016 (2004) 138.
[3] M. Lv, S. Li, J.J. Jasieniak, J. Hou, J. Zhu, Z. Tan, S.E. Watkins, Y. Li, X. Chen, Adv. Mater. 25 (2013) 6889.
[4] B.C.J. Brabec, A. Cravino, D. Meissner, N.S. Sariciftci, T. Fromherz, M.T. Rispens, L. Sanchez, J.C. Hummelen, Adv. Funct. Mater. 11 (2001) 374.
[5] S.S. Reddy, U.K. Aryal, H. Jin, T. Gokulnath, D.G. Rajalapati, K. Kranthiraja, S. T. Shin, S.H. Jin, Macromol. Res. 28 (2020) 179.
[6] S. Lee, J.W. Ha, H.J. Park, D.H. Hwang, Macromol. Res. (2020) 903.
[7] H. Cha, J. Li, Y. Li, S.-O. Kim, Y.-H. Kim, S.-K. Kwon, Macromol. Res. 28 (2020) 820.
[8] Z. Ma, B. Zhao, Y. Gong, J. Deng, Z. Tan, J. Mater. Chem. A 7 (2019) 22826.
[9] Y. Li, Acc. Chem. Res. 45 (2012) 723.
[10] W. Zhang, Y. Wu, Q. Bao, F. Gao, J. Fang, Adv. Energy Mater. (2014) 4.
[11] S.L. Handoko, H.C. Jin, D.R. Whang, J.H. Kim, D.W. Chang, J. Ind. Eng. Chem. 86 (2020) 244.
[12] S.L. Handoko, H.C. Jin, D.R. Whang, S.K. Putri, J.H. Kim, D.W. Chang, J. Ind. Eng. Chem. 73 (2019) 192.
[13] G. Yu, J. Gao, J. C. Hummelen, F. Wudl, A. J. Heeger, Science (80-.). 1995, 270, 1789.
[14] M.S. Abdullah, E.B. Akhtar, L. Kim, H.S. Fijahi, S.A. Shin, J. Ind. Eng. Chem. 81 (2020) 309.
[15] E.R. Rwenyagila, Int. J. Photoenergy 2017 (2017) 1.
[16] L.J.A. Koster, E.C.P. Smits, V.D. Mihailetchi, P.W.M. Blom, Phys. Rev. B 72 (2005), 085205.
[17] Y.J. Cheng, S.H. Yang, C.S. Hsu, Chem. Rev. 109 (2009) 5868.
[18] J. Jiang, H. Chen, H. Lin, C. Yu, S. Lan, Polym. Chem. 4 (2013) 5321.
[19] B.G. Dennler, M.C. Scharber, C.J. Brabec, Adv. Mater. 21 (2009) 1323.
[20] M. Kim, B. Kim, J. Kim, A.C.S. Appl, Mater. Interfaces 1 (2009) 1264.
[21] H. Chen, J. Hou, S. Zhang, Y. Liang, G. Yang, Y. Yang, Nat. Photonics 3 (2009) 649.

[22] C. Piliego, T.W. Holcombe, J.D. Douglas, C.H. Woo, P.M. Beaujuge, J.M.J. Fre, J. Am. Chem. Soc. 132 (2010) 7595.
[23] B.G. Zhao, Y. He, Y. Li, Adv. Mater. 22 (2010) 4355.
[24] J.H. Seo, A. Gutacker, Y. Sun, H. Wu, F. Huang, Y. Cao, U. Scherf, A.J. Heeger, G. C. Bazan, J. Am. Chem. Soc. 133 (2011) 8416.
[25] J. Yuan, L. Xiao, B. Liu, Y. Li, Y. He, C. Pan, Y. Zou, J. Mater. Chem. A 1 (2013) 10639.
[26] C. Duan, K. Zhang, C. Zhong, F. Huang, Y. Cao, Chem. Soc. Rev. 42 (2013) 9071.
[27] C. Chueh, C. Li, A.K. Jen, Energy 8 (2015) 1160.
[28] P. Shen, Y. Liu, Y. Long, L. Shen, B. Kang, J. Phys. Chem. C 120 (2016) 8900.
[29] P. Shen, G. Wang, B. Kang, W. Guo, L. Shen, A.C.S. Appl, Mater. Interfaces 10 (2018) 6513.
[30] H. Yip, A.K. Jen, Energy Environ. Sci. 5 (2012) 5994.
[31] T.T. Do, H.S. Hong, Y.E. Ha, S. Il Yoo, Y.S. Won, M.J. Moon, J.H. Kim, Macromol. Res. 23 (2015) 367.
[32] L. Zhang, C. Liu, T. Lai, H. Huang, X. Peng, F. Huang, J. Mater. Chem. A 4 (2016) 15156.
[33] Y.L. Li, Y.S. Cheng, P.N. Yeh, S.H. Liao, S.A. Chen, Adv. Funct. Mater. 24 (2014) 6811.
[34] S. Lee, D. Jeong, C. Kim, C. Lee, H. Kang, H.Y. Woo, B.J. Kim, ACS Nano 14 (2020) 14493.
[35] G. Li, R. Zhu, Y. Yang, Nat. Photonics 6 (2012) 153.
[36] Z. He, C. Zhong, X. Huang, W. Wong, H. Wu, Adv. Mater. 23 (2011) 4636.
[37] X. Zhang, X. Chen, S. Huang, X. Peng, Synth. Met. 253 (2019) 110.
[38] Z.A. Page, Y. Liu, V.V. Duzhko, Science (80-.). 2014, 346, 441.
[39] G. Xu, L. Gao, H. Xu, L. Huang, Y. Xie, X. Cheng, Y. Li, L. Chen, Y. Chen, J. Mater. Chem. A 5 (2017) 13807.
[40] S. Dong, K. Zhang, X. Liu, Q. Yin, H.L. Yip, F. Huang, Y. Cao, Sci. China Chem. 62 (2019) 67.
[41] H.C. Jin, S.A. Salma, D.K. Moon, J.H. Kim, J. Mater. Chem. A 8 (2020) 4562.
[42] Y.H. Kim, N. Sylvianti, M.A. Marsya, J. Park, Y.C. Kang, D.K. Moon, J.H. Kim, ACS Appl Mater. Interfaces 8 (2016) 32992.
[43] Y.H. Kim, D.G. Kim, R.D. Maduwu, H.C. Jin, D.K. Moon, J.H. Kim, Sol. RRL 2 (2018) 1800086.
[44] D.G. Kim, Y.H. Kim, R.D. Maduwu, H.C. Jin, D.K. Moon, J.H. Kim, J. Ind. Eng. Chem. 65 (2018) 175.
[45] M. Jeong, H.C. Jin, D.K. Moon, J.H. Kim, Adv. Mater. Interfaces 1900797 (2019) 1.
[46] M. Jeong, H.C. Jin, J.H. Lee, D.K. Moon, J.H. Kim, Dye. Pigment. 173 (2020), 107927.
[47] M.I. Arroyo-Villan, G.A. Diaz-Quijada, M.S.A. Abdou, S. Holdcroft, Macromolecules 28 (1995) 975.
[48] M. Ahmed, Ultra high resolution crystallography of small molecules and proteins, Université de Lorraine, 2018.
[49] B. Liu, W.L. Yu, Y.H. Lai, W. Huang, Chem. Commun. (2000) 551.
[50] C.D. Canestraro, P.C. Rodrigues, C.F.N. Marchiori, C.B. Schneider, L. Akcelrud, M. Koehler, L.S. Roman, Sol. Energy Mater. Sol. Cells 95 (2011) 2287.
[51] 2004 M.J. Frisch, G.W. Trucks, H.B. Schlegel, G.E. Scuseria, M.A. Robb, J.R. Cheeseman, J.A. Montgomery Jr., T. Vreven, K.N. Kudin, J.C. Burant, J.M. Millam, S.S. Iyengar, J. Tomasi, V. Barone, B. Mennucci, M. Cossi, G. Scalmani, N. Rega, G. A. Petersson, H. Na, Gaussian"16 {R}evision {C}.01 2016, Gaussian Inc. Wallingford CT.
[52] I. Franco, S. Tretiak, J. Am. Chem. Soc. 126 (2004) 12130.
[53] A. Mabrouk, A. Azazi, K. Alimi, Polym. Eng. Sci. 53 (2013) 1040.
[54] M. Knaapila, Z. Konôpková, M. Torkkeli, D. Haase, H.P. Liermann, S. Guha, U. Scherf, Phys. Rev. E - Stat. Nonlinear, Soft Matter Phys. 87 (2013) 1.
[55] J.H. Seo, Y. Jin, J.Z. Brzezinski, B. Walker, T.Q. Nguyen, ChemPhysChem 10 (2009) 1023.
[56] Z.G. Zhang, B. Qi, Z. Jin, D. Chi, Z. Qi, Y. Li, J. Wang, Energy Environ. Sci. 2014 (1966) 7.
[57] G.F. Burkhard, E.T. Hoke, M.D. McGehee, Adv. Mater. 22 (2010) 3293.
[58] X. Zhang, C. Hägglund, E.M.J. Johansson, Adv. Funct. Mater. 26 (2016) 1253.
[59] M. Al Mubarok, H. Aqoma, F. Tri, A. Wibowo, W. Lee, H.M. Kim, D.Y. Ryu, J. Jeon, S. Jang, Adv. Energy Mater. 1902933 (2020) 1.
[60] K. Zhang, B. Fan, R. Xia, X. Liu, Z. Hu, H. Gu, S. Liu, H.L. Yip, L. Ying, F. Huang, Y. Cao, Adv. Energy Mater. 8 (2018) 1.
[61] S. Kitova, D. Stoyanova, J. Dikova, M. Kandinska, A. Vasilev, S. Angelova, J. Phys. Conf. Ser. (2014) 558.
[62] C. Wang, Y. Luo, J. Zheng, L. Liu, Z. Xie, F. Huang, B. Yang, Y. Ma, ACS Appl Mater. Interfaces 10 (2018) 10270.
[63] K. Zilberberg, A. Behrendt, M. Kraft, U. Scherf, T. Riedl, Org. Electron. 14 (2013) 951.
[64] K. Bini, X. Xu, M.R. Andersson, E. Wang, ACS Appl Energy Mater. 1 (2018) 2176.
[65] Z. He, H. Wu, Y. Cao, Adv. Mater. 26 (2014) 1006.
[66] Y. Zhou, C. Fuentes-Hernandez, J. Shim, J. Meyer, A. J. Giordano, H. Li, P. Winget, T. Papadopoulos, H. Cheun, J. Kim, M. Fenoll, A. Dindar, W. Haske, E. Najafabadi, T. M. Khan, H. Sojoudi, S. Barlow, S. Graham, J. L. Brédas, S. R. Marder, A. Kahn, B. Kippelen, Science (80-.). 2012, 336, 327.
[67] S. Van Reenen, S. Kouijzer, R.A.J. Janssen, M.M. Wienk, M. Kemerink, Adv. Mater. Interfaces 1 (2014) 1.
[68] K.G. Lim, S.M. Park, H.Y. Woo, T.W. Lee, ChemSusChem 8 (2015) 3062.
[69] Z. Hu, K. Zhang, F. Huang, Y. Cao, Chem. Commun. 51 (2015) 5572.
[70] E.L. Ratcliff, B. Zacher, N.R. Armstrong, J. Phys. Chem. Lett. 2 (2011) 1337.
[71] J. Park, R. Yang, C.V. Hoven, A. Garcia, D.A. Fischer, T.Q. Nguyen, G.C. Bazan, D. M. Delongchamp, Adv. Mater. 20 (2008) 2491.
[72] M.Y. Jo, T.T. Do, Y.E. Ha, Y.S. Won, J.H. Kim, Org. Electron. 16 (2015) 18.
[73] M.Y. Jo, Y.E. Ha, Y.S. Won, S. Il Yoo, J.H. Kim, Org. Electron. 25 (2015) 85.
[74] Z. Yin, J. Wei, Q. Zheng, Adv. Sci. 3 (2016) 1.
[75] M. Young Jo, Y. Eun Ha, J. Hyun Kim, Sol. Energy Mater. Sol. Cells 107 (2012) 1.
[76] T.T. Do, J.H. Bae, S. Il Yoo, K.T. Lim, H.Y. Woo, J.H. Kim, Mol. Cryst. Liq. Cryst. 581 (2013) 31.
[77] Y.H. Kim, D.G. Kim, R.D. Maduwu, H.C. Jin, D.K. Moon, J. H. Kim 2 (2018) 1800086.
[78] A. Bagui, S.S.K. Iyer, Org. Electron. 15 (2014) 1387.
[79] S. Park, W. Jang, D.H. Wang, Macromol. Res. 26 (2018) 472.
[80] P. Shen, M. Yao, G. Wang, R. Mi, W. Guo, Y. Bai, L. Shen, J. Mater. Chem. A 6 (2018) 17401.
[81] B. Qi, Z.G. Zhang, J. Wang, Sci. Rep. 5 (2015) 1.
[82] X. Jia, Z. Jiang, X. Chen, J. Zhou, L. Pan, F. Zhu, Z. Sun, S. Huang, A.C.S. Appl, Mater. Interfaces 8 (2016) 3792.
[83] L. Gao, Z.G. Zhang, L. Xue, J. Min, J. Zhang, Z. Wei, Y. Li, Adv. Mater. 2016 (1884) 28.
[84] A. Gusain, R.M. Faria, P.B. Miranda, Front. Chem. 7 (2019) 61.
[85] S. Nho, G. Baek, S. Park, B.R. Lee, M.J. Cha, D.C. Lim, J.H. Seo, S.H. Oh, M.H. Song, S. Cho, Energy Environ. Sci. 9 (2016) 240.
[86] H. Liu, L. Huang, X. Cheng, A. Hu, H. Xu, L. Chen, Y. Chen, A.C.S. Appl, Mater. Interfaces 9 (2017) 1145.
[87] Y. Li, X. Li, X. Liu, L. Zhu, W. Zhang, J. Fang, J. Phys. Chem. C 120 (2016) 26244.
[88] K. Rainer, R. Sastrawan, J. Ferber, R. Stangl, J. Luther, Electrochim. Acta (2002) 4213.
[89] K.V. Sankar, R.K. Selvan, RSC Adv. 4 (2014) 17555.
[90] Q. Qu, P. Zhang, B. Wang, Y. Chen, S. Tian, Y. Wu, R. Holze, J. Phys. Chem. C 113 (2009) 14020.
[91] Y. Huang, Y. Li, Z. Hu, G. Wei, J. Guo, J. Liu, J. Mater. Chem. A 1 (2013) 9809.
[92] H. Toyohisa, K. Ryuji, S. Kazunari, E. Koichi, Electrochemistry 70 (2002) 675.